# Channel Estimation via Loss Field: Accurate Site-Trained Modeling for Shadowing Prediction

Jie Wang, Meles G. Weldegebriel, and Neal Patwari
McKelvey School of Engineering
Washington University in St. Louis, Missouri, USA

***Abstract*—Future networks which share spectrum dynamically among groups of mobile users will require fast and accurate channel estimation in order to guarantee signal-to-interference-plus-noise ratio (SINR) requirements for co-channel links. There is a need for channel models with low computational complexity and high accuracy that adapt to the particular area of deployment while preserving explainability. We propose the *Channel Estimation via Loss Field (CELF)* model, which uses channel loss measurements from a deployed network and a Bayesian linear regression method to estimate a site-specific loss field for the area. The loss field is explainable as a site map of additional radio 'shadowing', compared to a base channel model, but it requires no site-specific terrain or building information. For an arbitrary pair of transmitter and receiver positions, CELF sums the loss field near the link line to estimate its shadowing loss. We use extensive measurements to show that CELF lowers the variance of channel estimates by up to 56% compared to the path loss exponent model, and outperforms 3 popular machine learning methods in variance reduction and training efficiency. CELF offers a new type of explainable learning model for accurate and fast site-specific radio channel loss estimation.**

***Index Terms*—channel modeling, shadowing prediction, dynamic spectrum assignment**

## I. Introduction

Spectrum allocation is becoming increasingly dynamic and shareable in order to meet the growing demand [1], [2]. Examples include the citizens broadband radio service (CBRS) band [3], and the radio dynamic zone [4], [5]. A major part of the challenge to achieve reliable dynamic spectrum allocation is to accurately and efficiently predict signal and interference powers between all pairs of proximate mobile transmitters and receivers, as shown in Fig. 1, to ensure that signal-to-interference-plus-noise ratios (SINRs) are sufficient for all groups.

Current channel models are not well-matched to the needs of dynamic spectrum management in mobile networks. Many path loss prediction models require computing losses due to propagation mechanisms such as reflection and diffraction in the particular geometry of the network deployment area. For example, the terrain-integrated rough earth model (TIREM) [6] computes diffraction losses based on the terrain features and building heights extracted for each transmitter and receiver pair. Ray tracing models [7] additionally require high-resolution environmental databases and are highly computationally complex. Such site-specific models have high accuracy compared to general-purpose models which curve-fit to empirical data, such as the Okumura-Hata [8] and log-distance path loss [9] models. However, if real-time dynamic spectrum management requires high-resolution site clutter data and significant computational resources, it will limit who can perform this management [10].

Contact: {jie.w, npatwari}@wustl.edu. This research is supported in part by the NSF grants #2232464 and #1827940, and the PAWR Project Office.

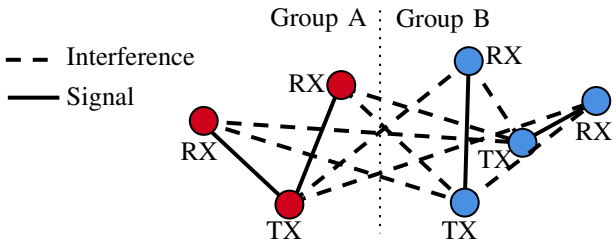


Fig. 1: Assigning channels and transmit powers to ensure the required SINRs among links between $T$ transmitters (TX) and $R$ receivers (RX) demands $RT$ channel loss estimation and recomputation as users move.

Emerging machine learning (ML) channel models can be both accurate and fast during testing but require very large datasets and computational resources during model training [11], [12]. Further, ML models suffer from the black-box problem, in which no human-understandable explanation or reasoning for their predictions is possible [13]. This prevents system engineers from diagnosing problems when a model performs poorly. Updating an ML channel model over time does not allow engineers to explain how (or if) the model has been impacted by changes in the environment, e.g., a new building having been constructed. Current and future regulations may require model explanations for legal purposes [14] — if some system is harmed by path loss prediction model errors, a human-understandable explanation must be provided.

In this paper, we develop and validate a new type of channel learning model, the Channel Estimation via Loss Field (CELF) model, which simultaneously is more accurate than current ML channel models trained with the same data, is explainable, and is less computationally complex to train. CELF formulates the link fading loss as a linear function of a shadowing loss field. This loss field is connected to the underlying wave propagation physics in that it accounts for the physical mechanism of shadowing due to obstacles in the spatial domain, and is

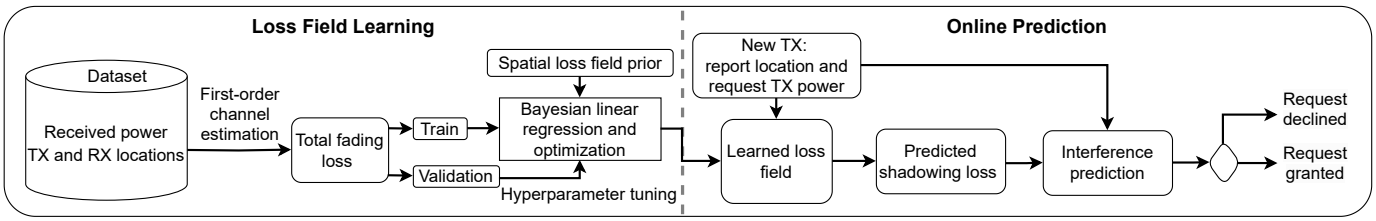


Fig. 2: Overview of the proposed CELF model and the online shadowing prediction process.

viewable as a simple image map. Research also estimates the shadowing attenuation caused by people [15] and walls [16] via this type of model. As shown in Fig. 2, the loss field is learned from training measurements via Bayesian linear regression, but training is lower in computation requirements compared to a general-purpose ML model. Using training measurements allows the model to fit the particular site of deployment. Sensors deployed as part of a radio dynamic zone, or conducted by nodes using the spectrum as part of the dynamic spectrum access protocol, can be used to collect these measurements. Training data quantities can be low in comparison with other ML methods. We also discuss Bayesian regression's stability and optimization for more robust and efficient learning of the loss field. To predict shadowing loss for a new link, CELF computes a weighted sum of a small number of voxels of the learned loss field image. The implementation of CELF is in [17].

We use outdoor and indoor datasets to experimentally quantify how accurately and efficiently CELF performs. We compare CELF with three general-purpose ML methods: support vector regression (SVR), random forests, and multi-layer perceptron (MLP)-ANN, in terms of (1) variance reduction compared to a baseline model, (2) training efficiency, and (3) prediction efficiency. CELF reduces the variance of total fading loss estimates by up to 56% outdoors and 40% indoors. In comparison to the ML-based methods, CELF achieves larger variance reductions. The MLP-ANN model is the most accurate model out of the three ML-based methods, but it requires three times more time than CELF for model training. For shadowing loss prediction, CELF is faster than SVR but slower than MLP-ANN as the test dataset size and the loss field size severely impact CELF's prediction efficiency.

For perspective, path loss models *do not predict small-scale fading effects*, i.e., those caused by sub-wavelength (cm-level) changes in the position of the transmitter or receiver. Small-scale fading is severe, e.g., more than 20 dB 1% of the time in a Rayleigh fading channel [9]. Path loss models do not know the device and environmental obstruction positions to the required level of accuracy. Instead, channel path loss models like our proposed model predict large-scale fading (caused by increasing distance) and medium-scale or shadow fading (caused by obstructions) [18]. Since training and testing measurements include small-scale fading but our model cannot predict it, we cannot reduce the path loss variance to zero. Instead, we judge models by how much they can reduce fading variance compared to a standard statistical channel model. We find that CELF shows larger variance reductions across all of our experiments, than any other model, ML or otherwise.

## II. Related Work

Path loss prediction has an extensive disciplinary history over several decades. Models used today vary by to what they rely on:

1) the physical mechanisms of radio propagation, e.g., reflection and diffraction;
2) information about the site, e.g., terrain and building geometry data;
3) curve-fitting to empirical data recorded in past measurements;
4) fitting or learning using empirical data collected in the area of deployment.

While some models do not characterize the probability distribution of the channel loss, *statistical models* state a distributional model for the loss variation.

### A. Physics-based models

Physics-based models aim to accurately characterize radio wave propagation effects such as reflection and diffraction. The most fundamental is the *free-space path loss model* [9], but it models only unobstructed channels, and is thus limited to satellite communication and unobstructed microwave relay links. The *two-ray ground reflection model* accounts for both the line-of-sight (LOS) and the ground-reflected paths [19], and is typically used in flat clutter-free areas like plains [20]. When more multipath must be modeled, *ray tracing* is both the most accurate and most complicated model for path loss [7]. Ray tracing requires site-specific building databases, i.e., building layout, heights, and dielectric properties, as well as detailed terrain and ground use data, so that each wave path can be traced using geometrical optics [21]. Its computational complexity and need for high-resolution site-specific data make it impractical for large-scale, real-time applications.

### B. General empirical models

General empirical models are based on an analysis of measurements taken from an environment similar in use to the area of interest, e.g., urban or suburban. The *Okumura-Hata model* is based on measurements from Tokyo in the 1960s as formulated by Hata [8]. It uses curve-fitting to model the effect of signal frequency, antenna heights, path length, and environment type on the channel loss. The *COST-231 Hata*

*model* extends the Okumura-Hata model to data from some European cities [22].The benefits of statistical models are the simple closed-form formula and no need for data from the site of interest. However, they are restricted to certain frequency and distance ranges, and most critically, they are most accurate in the environments from which the measurements came [20].

### C. Hybrid empirical/physical models

The *Longley-Rice model* and the irregular terrain model (ITM) combine empirical modeling and physical principles for ground reflection, knife-edge and far-field diffraction, and troposcatter predictions [23]. This model considers environmental factors including surface refractivity, ground conductivity, atmospheric parameters, and terrain irregularities for path loss prediction [7]. It is in use today in systems like SAS [24]. The terrain-integrated rough Earth model (TIREM) model [6] considers a profile of the terrain features and building heights [25]. The last hybrid model is the International Telecommunication Union's (ITU)-R P.1812 model, which uses detailed terrain profiles to target path-specific predictions. It has been widely used for terrestrial wireless systems [26].

### D. Statistical models

Statistical models characterize the statistical distribution of the channel losses, rather than only the average value. The most common model is the *log-normal shadowing model*, which models shadowing loss as normally distributed in dB [20]. Other models explain the statistical correlation between the shadowing loss on two proximate links [27]–[29], which become correlated by passing through the same or similar obstructions. CELF models this correlation implicitly via its loss field. Other distributions for shadowing include the *Gamma* [30] and *inverse Gamma* [31] distributions. We note that the most well-known distributions, Rayleigh and Rician, are models for small-scale fading loss, and are thus not further discussed in this paper.

### E. ML channel models

Another popular class is ML channel models which are designed using general-purpose ML architectures and extensive datasets [11], [32], [33]. We categorize these models as: (1) SVR, K-Nearest-Neighbors (KNN), and ensemble learning methods such as random forests [33]; (2) ANN models including MLP-ANN models [34], [35] and radial basis function-ANN models (RBF-ANN) [36], and (3) more complex DNN models [12], [37]. For example, the RadioUNet model in [12] utilizes large datasets and environmental geometry as input to Unet, a special Convoluted Neural Network (CNN) architecture for path loss modeling.

ML-based methods can provide higher prediction accuracy than domain-specific models at the cost of extensive datasets or detailed environmental information. Additionally, the high complexity of model training and updating will result in significant latency. The lack of interpretability of ML methods is a particular challenge, as RF engineers can find it difficult to diagnose a problem when the model performs poorly. Further, regulation increasingly requires businesses to be able to explain why an algorithm's prediction was made [14].

CELF is also a learning-based model which uses site measurements to train. It requires no knowledge about the environment and can be trained with fewer measurements than a general-purpose ML model. Further, CELF explains its estimates via the shadowing field image, which should correlate to the attenuating obstructions in the area.

## III. Channel Estimation via Loss Field

In this section, we present the CELF model in three parts. First, we describe the idea of a base model, and describe what is used in this paper. Next, we describe how CELF augments the base model for better path loss estimation, using a spatial loss field. Finally, we explain how to estimate the loss field from training measurements.

### A. First-order channel estimation

CELF predicts the additional path loss compared to a *base model*, an arbitrary path loss model. The base model could be any model described in the related work (Section II), but presumably something simple to compute. CELF's role is to augment the estimates from the base model by additionally accounting for the natural spatial correlations in the path loss.

In this paper, we use the *log-distance path loss* model as the base model, which states that the ensemble average power $\bar{P}(d_l)$ along a link $l = (i, j)$ between node $i$ and node $j$ reduces in a logarithmic manner with increasing distance [9]:

$$\bar{P}(d_l) = P_T - \Pi_0 - 10 n_p \log \frac{d_l}{\Delta_0} \tag{1}$$

where $P_T$ is the transmitted power in dBm, $d_l$ is the link distance, $\Pi_0$ is a constant specifying the dB loss at a reference distance $\Delta_0$, and the path loss exponent $n_p$ indicates the level of environmental clutter.

Given the same distance $d_l$, the received power measurements vary around the average $\bar{P}(d_l)$ due to shadow fading and small-scale fading [20]. As a result, the received power $P(d_l)$ along the link $l$ can be written as:

$$\begin{aligned} P(d_l) &= \bar{P}(d_l) - Z_l \\ Z_l &= X_l + Y_l, \end{aligned} \tag{2}$$

where $Z_l$ is the total fading loss, which consists of independent shadowing loss $X_l$ and small-scale fading loss $Y_l$ [15].

### B. Network shadowing model for shadowing correlation

The total fading loss $Z_l$ is commonly modeled as independent and identically distributed ($i.i.d.$) across links [38]–[40]. However, that simplification disagrees with the empirical observation that shadowing losses along two links are correlated due to obstructions, e.g., outdoor buildings and terrain variations, and indoor walls and furniture [28], [41], [42].

In order to simultaneously model the correlations in shadow fading that exist across multiple link pairs in a network, we use the network shadowing model [43]. Let $\mathcal{L}$ be a set of link pairs in a wireless network, and $L = |\mathcal{L}|$ is the size of the set.

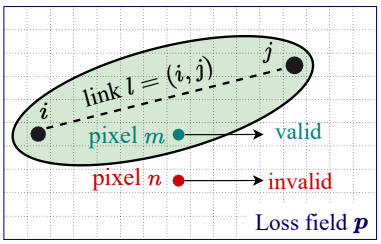


Fig. 3: The ellipse model for selecting valid pixels (•) that contribute to the shadowing loss of link $l = (i, j)$.

We assume that each link is different in either transmitter or receiver location from the other links in the set $\mathcal{L}$. The network shadowing model describes the joint link fading loss as:

$$\boldsymbol{z} = \boldsymbol{W}\boldsymbol{p} + \boldsymbol{n} \tag{3}$$

where $\boldsymbol{z} = [Z_1, Z_2, \ldots, Z_L]^T \in \mathcal{R}^{L\times 1}$ is the total fading loss vector, $\boldsymbol{W} \in \mathcal{R}^{L\times M}$ is a weight matrix, $\boldsymbol{p} \in \mathcal{R}^{M\times 1}$ is a discretized loss field in dB, and $\boldsymbol{n} \in \mathcal{R}^{L\times 1}$ is a noise vector. Their details are given below.

**Spatial loss field**. The spatial loss field of [43] characterizes the environment of interest as a Gaussian random field that is isotropic wide-sense stationary. It has zero mean and an exponentially decaying spatial covariance function:

$$C_p(m, n) = \frac{\sigma_X^2}{\delta} \exp(-\frac{d_{m,n}}{\delta}) \tag{4}$$

where $d_{m,n}$ is the Euclidean distance between the centers of pixels $m$ and $n$, $\sigma_X^2$ is the variance of the shadowing loss, and $\delta$ is a space constant.The shadowing loss $Z_l$ on link $l$ is then a weighted sum of the loss field $\boldsymbol{p}$ over the pixels that cross near the link $l$.

**Weight matrix model**. A popular ellipse model in [15] is adopted for the weight matrix $\boldsymbol{W}$, as shown in Fig. 3. It considers the two ends of link $l$ as the foci and utilizes a tunable parameter $\lambda$ to determine the ellipse width. A pixel is viewed as valid if it falls within the ellipse, and the corresponding weight in $\boldsymbol{W}$ will have a non-zero contribution to the shadowing loss of link $l$. Past studies [15], [42], [43] construct the weight as:

$$w_{lm} = \frac{1}{\sqrt{d_l}} \begin{cases} 1, & \text{if } d_{l,m}(1) + d_{l,m}(2) < d_l + \lambda \\ 0, & \text{otherwise} \end{cases} \tag{5}$$

where $d_{l,m}(1)$ and $d_{l,m}(2)$ are the distances from the center of pixel $m$ to the two ends of link $l$, $d_l$ is the link distance, and $\lambda$ is the ellipse width parameter.

**Small-scale fading and noise**. The Gaussian noise $\boldsymbol{n}$ is the sum of small-scale fading loss and measurement noise which are independent of each other. Measurement noise is first assumed to be $i.i.d.$ normally distributed. Small-scale fading, also known as multipath fading, describes the attenuation that occurs from constructive and destructive addition of multipath phasors [20]. While small-scale fading may have multiple distributions depending on the number of significant-amplitude multipath components [44], here we model it as $i.i.d.$ Gaussian in dB. The rationale is in [42] which approximates small-scale fading to be (1) uncorrelated for mobile network nodes that are typically many wavelengths separated and (2) Gaussian distributed by averaging it across many frequencies. Note that without the Gaussian noise assumption, Bayesian linear regression still applies for loss field learning and the analytical solution given below can be adjusted accordingly.

### C. Loss field learning

**Bayesian linear regression**. Given the linear joint link model in (3) and the Gaussian loss field prior, we reconstruct the loss field $\boldsymbol{p}$ via Bayesian linear regression. We note the likelihood function of the total fading loss vector is,

$$f(\boldsymbol{z}|\boldsymbol{W}, \boldsymbol{p}, \sigma_n^2) = \mathcal{N}(\boldsymbol{W}\boldsymbol{p}, \sigma_n^2 \boldsymbol{I}_L). \tag{6}$$

Next, the loss field prior is modeled as Gaussian with pdf,

$$f(\boldsymbol{p}) = \mathcal{N}(\boldsymbol{0}, \boldsymbol{C}_{\boldsymbol{p}}). \tag{7}$$

Therefore the posterior pdf of $\boldsymbol{p}$ is multivariate Gaussian as

$$\begin{aligned} f(\boldsymbol{p}|\boldsymbol{z}, \boldsymbol{W}, \sigma_n^2) &\propto f(\boldsymbol{z}|\boldsymbol{W}, \boldsymbol{p}, \sigma_n^2) \cdot f(\boldsymbol{p}) \\ &= \mathcal{N}(\boldsymbol{\mu}_{\boldsymbol{p}|\boldsymbol{z}}, \boldsymbol{C}_{\boldsymbol{p}|\boldsymbol{z}}), \end{aligned} \tag{8}$$

where

$$\begin{aligned} \boldsymbol{\mu}_{\boldsymbol{p}|\boldsymbol{z}} &= \sigma_n^{-2}(\sigma_n^{-2}\boldsymbol{W}^T\boldsymbol{W} + \boldsymbol{C}_{\boldsymbol{p}}^{-1})^{-1}\boldsymbol{W}^T\boldsymbol{z}, \\ \boldsymbol{C}_{\boldsymbol{p}|\boldsymbol{z}} &= (\sigma_n^{-2}\boldsymbol{W}^T\boldsymbol{W} + \boldsymbol{C}_{\boldsymbol{p}}^{-1})^{-1}. \end{aligned} \tag{9}$$

As a result, we can acquire both the minimum mean-square error (MMSE) solution and the maximum a posterior (MAP) estimator $\hat{\boldsymbol{p}}$ as the posterior mean $\boldsymbol{\mu}_{\boldsymbol{p}|\boldsymbol{z}}$ in (9).

The solution can be further generalized by a tunable regularizer $\alpha$, which leads to the final estimator $\hat{\boldsymbol{p}}$ as:

$$\begin{aligned} \hat{\boldsymbol{p}} &= \Pi_1 \boldsymbol{z} \\ \Pi_1 &= (\boldsymbol{W}^T\boldsymbol{W} + \alpha \boldsymbol{C}_{\boldsymbol{p}}^{-1})^{-1}\boldsymbol{W}^T \end{aligned} \tag{10}$$

**Solution stability**. The linear regression, however, is an ill-posed problem, i.e., the attenuation image estimate $\hat{\boldsymbol{p}}$ from the measurement vector is not unique. Such ill-posedness is due to two main factors:

1) $L < M$: there are more pixels to be estimated than link measurements, thus the problem is underdetermined;
2) $L > M$ but with a sparse $\boldsymbol{W}$: only a few pixels are assigned non-zero weights for each link and thus $\boldsymbol{W}$ is rank-deficient regardless of the number of link samples.

For a stable solution, the regularization constant $\alpha$ in (10) is required to be positive. In doing so, the estimator is robust to rank deficiency in the weight matrix, and the inverse term in the operator $\Pi_1$ always exists.

**Solution efficiency**. Latency can be the other concern given large datasets and wide area estimation, and thus requires efficiency improvement. If $L < M$, we can review the problem as sparse linear regression and adopt the common minimum norm estimator (MNE) as:

$$\begin{aligned} \hat{\boldsymbol{p}} &= \Pi_2 \boldsymbol{z} \\ \Pi_2 &= \boldsymbol{C}_{\boldsymbol{p}}\boldsymbol{W}^T(\boldsymbol{W}\boldsymbol{C}_{\boldsymbol{p}}\boldsymbol{W}^T + \alpha \boldsymbol{I})^{-1} \end{aligned} \tag{11}$$

| Dataset | Receiver | Count | SDR | Antenna Height (m) | Samples |
|---|---|---|---|---|---|
| Outdoor | Rooftop | 5 | X310 | 28–51 | 13114 |
| | Fixed | 12 | B210 | 1.5 | 24253 |
| | Mobile | 7 | B210 | 2.0 | 8688 |
| | Dense | 5 | B210 | 8.8 | 13268 |
| Indoor | DS-SS | 44 | – | 1.0 | 946 |

TABLE I: Specifications for the indoor and outdoor datasets.

which calculates an inverse of only a $\mathcal{R}^{L\times L}$ matrix rather than $\mathcal{R}^{M\times M}$.

If $L > M$, we leverage the Cholesky decomposition [45] to lower the latency. It is based on the fact that $(\boldsymbol{W}^T\boldsymbol{W}+\alpha\boldsymbol{C}_{\boldsymbol{p}}^{-1})$ in $\Pi_1$ is symmetric and positive definite. Let $\boldsymbol{A} = \boldsymbol{W}^T\boldsymbol{W} + \alpha\boldsymbol{C}_{\boldsymbol{p}}^{-1}$, and $\boldsymbol{b} = \boldsymbol{W}^T\boldsymbol{z}$. We first calculate the triangular matrix $\boldsymbol{S}$ via the Cholesky factorization:

$$\boldsymbol{S}\boldsymbol{S}^T = \boldsymbol{A}, \quad \boldsymbol{S} = \text{chol}\boldsymbol{A}. \tag{12}$$

By reformulating the problem as $\boldsymbol{S}\boldsymbol{S}^T\boldsymbol{p} = \boldsymbol{b}$, the loss field estimate $\hat{\boldsymbol{p}}$ can be obtained via forward-backward substitution. According to [46], the Cholesky decomposition can be twice as efficient as the general LU decomposition.

## IV. Evaluation Methodology

In this section, we describe one outdoor and one indoor real-world received power dataset, three popular ML-based methods, and two evaluation metrics for assessing the performance of the CELF algorithm.

### A. Real-world received power datasets

**Outdoor Dataset.** This dataset [47] is collected from a 2.2 km $\times$ 2.1 km university campus area. A portable commercial radio is used as the transmitter, and the receivers are 25 software-defined radio (SDR) nodes with omnidirectional antennas deployed on POWDER, an open wireless experimental testbed [48]. The carrier frequency is 462.7 MHz and the transmit power is 1W. The receivers are one of 4 types, *Rooftop, Fixed, Mobile, and Dense*, according to the radio-antenna-placement differentiation. Table I gives specifications for each receiver type. Fig. 4a and 4b show the GPS coordinates of the transmitter and all the receivers on the campus map. As the four types of receivers are heterogeneous and uncalibrated, this work treats the data collected by each type as a separate dataset.

**Indoor Dataset.** This dataset [49] is from in an indoor office area, a 17.5 m $\times$ 15 m space surrounded by 1.8 m high cubicle walls, as shown in Fig. 4c. Channels between all pairs of 44 device locations are measured by transmitting a pseudo-noise code with a 40-MHz chip rate at 2443 MHz. The transmit power is 10 mW. Thus, this indoor dataset has in total $44 \times 43 \times 0.5 = 946$ measurements assuming link reciprocity, as described in [50].

**Train-Test Split.** Each dataset needs to be split without overlapping for loss field estimation (training) and shadowing loss prediction (testing) purposes. We choose the link index as the criterion to partition the datasets. Each dataset is split with a 7: 3 ratio. Each data point is randomly assigned for training or testing.

### B. Methods for comparison

We adopt the *Okumura-Hata model* and three general-purpose ML models, *Random Forest, SVR, and MLP-ANN*, in this work for performance comparison. The rationale behind such choices is: (1) they represent the two main categories in the related work – non-learning and learning approaches; (2) they require neither site-specific terrain information nor large-scale datasets, unlike complex deep learning models such as RadioUNet [12] and PL-GAN [51]; (3) they have been widely used as benchmarks for path loss prediction [20], [33], [34], [52], and the *Okumura-Hata model* particularly has been in use for the CBRS band sharing and analysis [53].

- *Okumura-Hata* [8]: it provides a closed-form empirical formula for path loss computation over 150-1500 MHz frequency range. This model is only compared across outdoor datasets as it does not capture indoor environments.
- *Random Forest* [54]: it is an ensemble learning approach that first constructs multiple decision trees on random subsets of the dataset and then combines them to improve the accuracy and robustness of the model.
- *SVR* [55]: it is a variation of support vector machines used for regression. Unlike traditional squared error minimization, SVR fits a line or a curve by maximizing the margin of error.
- *MLP-ANN* [34]: MLP-ANN is a feedforward neural network that consists of an input layer, an output layer, and multiple hidden layers. It is trained iteratively using algorithms like stochastic gradient descent for squared error optimization.

### C. Evaluation metrics

We adopt two evaluation metrics, *variance reduction* and *running time*, to quantify the performance of the tested algorithms. To specify, *variance reduction* is defined as the percentage decrease of the fading loss variance, i.e.,

$$\epsilon = \frac{\sigma^2_{\boldsymbol{z}_\mathcal{T}} - \sigma^2_{\text{err}}}{\sigma^2_{\boldsymbol{z}_\mathcal{T}}} \cdot 100\% \tag{13}$$

where $\sigma^2_{\boldsymbol{z}_\mathcal{T}}$ is the fading loss variance of a dataset $\mathcal{T}$ after the first-order channel estimation in Section III-A, and $\sigma^2_{\text{err}}$ is the error variance after shadowing loss subtraction which is computed as the mean-squared error (MSE):

$$\sigma^2_{\text{err}} = \frac{\|\boldsymbol{z}_\mathcal{T} - \boldsymbol{W}_\mathcal{T} \cdot \hat{\boldsymbol{p}}\|^2}{N_\mathcal{T}} \tag{14}$$

where $\hat{\boldsymbol{p}}$ is the attenuation image learned from Section III-C, $\boldsymbol{W}_\mathcal{T}$ is the weight matrix using the ellipse model, and $N_\mathcal{T} = |\mathcal{T}|$ is the size of the dataset $\mathcal{T}$.

The other metric, *running time*, is a measure of the computational efficiency of the proposed CELF algorithm. It has been crucial in time-sensitive applications such as real-time spectrum access and management systems [56]. This

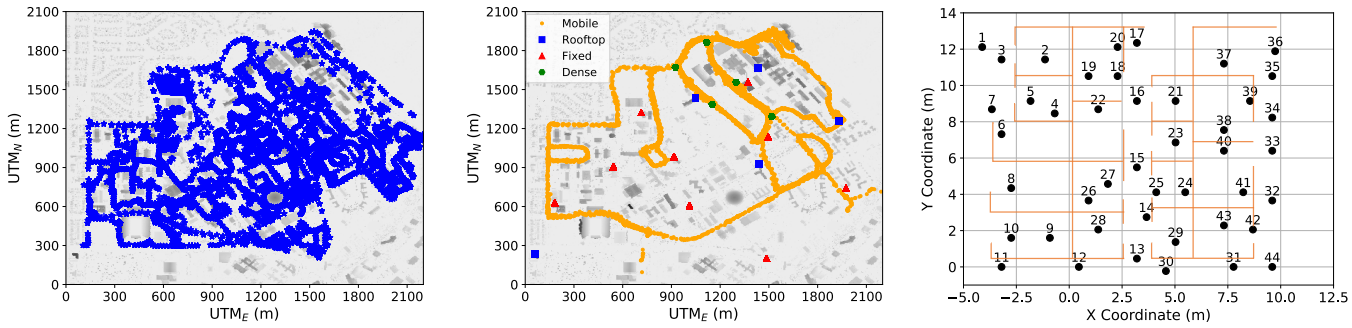


(a) The outdoor transmitter locations (b) The outdoor receiver locations (c) The 44 indoor node locations

Fig. 4: The transmitter and receiver locations of the outdoor and indoor received power datasets. They are collected in a 2200×2100 m$^2$ campus area and a 17.5×15 m$^2$ indoor office with cubicles (–) respectively.

metric includes the execution time for loss field learning and shadowing loss prediction. Note that the terms "learning" and "training", "prediction" and "testing" are used interchangeably for comparing CELF to the selected approaches in Section V.

We take the following three steps to ensure result comparability. First, all the models are trained and tested on the same partitioned datasets. Second, the inputs of these ML models are the 2D coordinates of transmitters and receivers to be consistent with CELF. Lastly, all the results are obtained by running the algorithm on the same Linux system with a 16-core Intel Xeon Gold 6130 processor.

## V. Results

Experimental results of the proposed CELF algorithm are given in this section. We first present two loss field image examples which are learned from the datasets in Section IV-A. We then compare CELF with the chosen models via *variance reduction and latency* from Section IV-C. The impact of the hyperparameters on accuracy is also discussed. Finally, we present results on the measurement noise variance and the small-scaling fading loss variance. The combination of the two approximates the total noise variance as a lower bound for the fading loss variance.

### A. Example loss field images

This subsection presents two example loss field images using the *log-distance path loss* model in Section III-A and the proposed CELF algorithm in Section III-C. They are learned from the *Rooftop* outdoor and indoor training datasets respectively. The rationale behind the *Rooftop* dataset choice is that these receivers, as deployed high above the ground, give better coverage of the campus area. We select both outdoor and indoor datasets to discuss CELF's practical use in various types of environments. The image boundaries are the same as Fig. 4a and 4c.

The statistical analysis follows the next four steps. First, we determine the path loss exponent $n_p$ and the reference loss $P_T - \Pi_0$ in (1) via linear regression. The reference distance $\Delta_0$ is set to be 1 m across the datasets. The results of the two examples are (1) *Rooftop*: $n_p = 2.73$ and $P_T - \Pi_0 = -1.25$ dBm, and (2) indoor: $n_p = 2.26$ and $P_T - \Pi_0 = -37.04$ dBm.

| Hyperparameter | Description | *Rooftop* | Indoor |
|---|---|---|---|
| $\delta_p$ | Pixel width (m) | 25 | 0.35 |
| $\sigma_{\boldsymbol{x}}^2/\sigma_{\boldsymbol{z}}^2$ | Shadowing variance ratio | 0.58 | 0.30 |
| $\delta$ | Space constant (m) | 35 | 2.5 |
| $\lambda$ | Excess length (m) | 105 | 0.18 |
| $\alpha$ | Regularization | 0.3 | 41 |

TABLE II: Model hyperparameters for CELF.

Second, we tune hyperparameters for CELF and interpret their values. The model hyperparameters are selected via 5-fold cross-validation. This procedure is to randomly sample $1/5$ data out of the training dataset for hyperparameter validation and overfitting prevention. Their descriptions and values are given in Table II. The first hyperparameter, $\delta_p$, denotes the attenuation image resolution and impacts both computation time and prediction accuracy. The second shadowing variance ratio, $\sigma_{\boldsymbol{x}}^2/\sigma_{\boldsymbol{z}}^2$, represents the contribution of shadowing loss to the total fading loss. In comparison to outdoor environments, indoor surroundings have more multipath components as indoor obstacles like walls that obstruct radio wave propagation are relatively uniformly placed throughout the area. Therefore the indoor dataset shows less variation in shadowing. The third space constant $\delta$ indicates the obstruction size in the environment [42]. We expect that obstacles will be smaller for the indoor area. In this case, the $\delta$ for the *Rooftop* dataset is 35, larger than 2.5 for the indoor dataset. The next hyperparameter $\lambda$ is introduced by the ellipse weight model to select valid pixels for each link. It is determined by the area size and the pixel width. The last hyperparameter $\alpha$ balances the loss field prior and the data from the area of interest. We notice that $\alpha$ of the indoor dataset is about 100 times larger than that of the outdoor case. This can be explained by the $1/\sqrt{d_l}$ weight in 5. The path lengths $d_l$ of the indoor measurements are 100 times smaller, which makes $\alpha$ 100 times larger to balance the $1/d_l$ discrepancy in 10.

Next, we derive the weight matrix and estimate the loss image via Bayesian linear regression. Fig. 5 demonstrates the

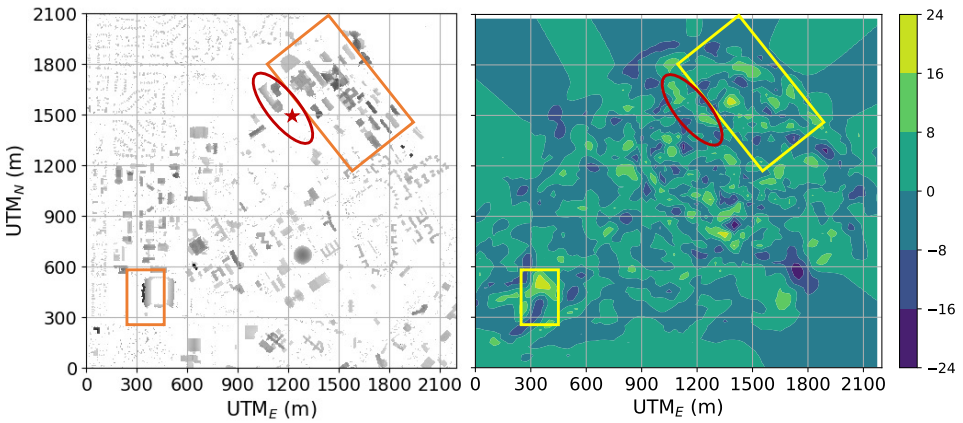


(a) The *Rooftop* training dataset.

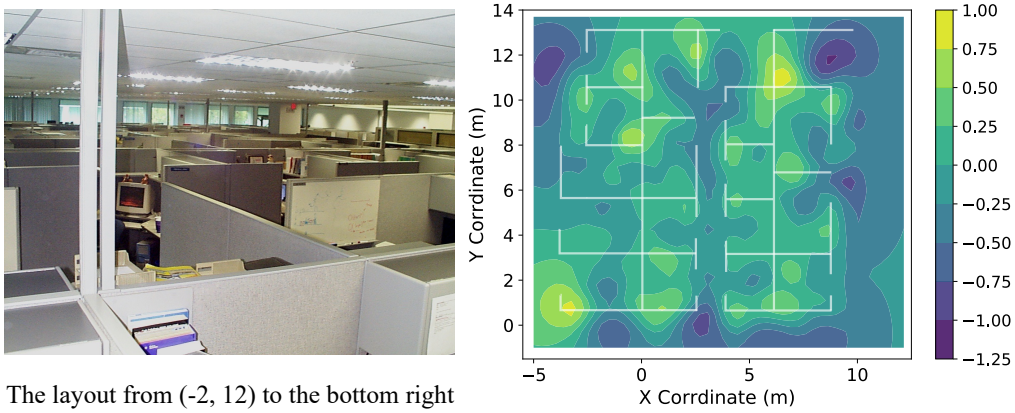


The layout from (-2, 12) to the bottom right

(b) The indoor training dataset.

Fig. 5: Example loss images learned via the proposed CELF algorithm and the site maps as a reference.

two trained loss images and the site maps as a reference. It can be observed that they have spatial loss ranges of -24–24 dB and -1.25–1.00 dB respectively. Higher losses can be seen at higher obstructions such as the marked rectangle areas in Fig. 5a and near cubicle walls in Fig. 5b.

The red ellipse area of Fig. 5a highlights a mismatch between the estimated two high-loss regions and one high obstruction of the site map. The loss image estimate is in fact more accurate because the terrain profile is outdated; a new building recently constructed at the star ($\star$) location was not in the database used to generate the left image in Fig. 5a. Note that CELF does not use any terrain or building information. Collecting and maintaining the site-specific terrain dataset could be time-consuming and expensive, but CELF can use channel loss measurements for accurate and cost-effective loss field estimation.

The correlation between obstructions and spatial losses is further proposed for wall imaging [16]. Fig. 5b presents the loss image of the indoor office and the cubicle locations. It can be observed that desks, computers, and bookcases are generally positioned close to the cubicle walls. Correspondingly the estimated loss image is lower in the middle of each cubicle and higher close to the cubicle walls where these obstructions are more often placed. Similarly, the vertical corridor region at $x \approx 3.2$ m experiences lower losses than either side of the corridor. The edges of the loss image are generally close to zero due to the lack of measurements and thus the estimates in that region mostly rely on the field prior. The match between the environment and the loss image validates that the proposed CELF approach has the potential for spatial loss field learning and further shadowing loss prediction.

The final step is to quantitatively assess the accuracy of the learned loss image via variance reduction. For the *Rooftop* training dataset, the fading loss variance after the *log-distance path loss model* is 58.4 dB$^2$. The MSE by estimating the shadowing loss decreases to 30.7 dB$^2$ which is 47.4% less than that of the base model. For the indoor training dataset, the fading loss variance reduces from 19.8 dB$^2$ to 10.1 dB$^2$, which corresponds to a 49.3% reduction.

### *B. Accuracy analysis*

Upon obtaining the loss image, we evaluate CELF's performance on the test datasets. The first is the accuracy analysis using the variance reduction metric. Fig. 6 demonstrates the variance reduction results on the outdoor and indoor test

| Receiver | Training Time (s) | | | | Testing Time (s) | | | | |
|---|---|---|---|---|---|---|---|---|---|
| | Random Forest | SVR | MLP-ANN | CELF | Okumura-Hata | Random Forest | SVR | MLP-ANN | CELF |
| Rooftop | 1.210 | 7.411 | 26.753 | 8.215 | 0.001 | 0.018 | 0.726 | 0.011 | 0.402 |
| Fixed | 1.587 | 28.687 | 59.671 | 15.767 | 0.001 | 0.027 | 2.353 | 0.024 | 0.642 |
| Mobile | 1.605 | 4.247 | 13.552 | 4.837 | 0.001 | 0.014 | 0.311 | 0.004 | 0.243 |
| Dense | 0.700 | 7.105 | 25.524 | 6.036 | 0.001 | 0.014 | 0.755 | 0.005 | 0.357 |
| DS-SS | 0.131 | 0.041 | 2.402 | 0.133 | – | 0.007 | 0.006 | 0.002 | 0.005 |

TABLE III: Running time comparison for training and testing among *Okumura-Hata*, ML models and the CELF algorithm.

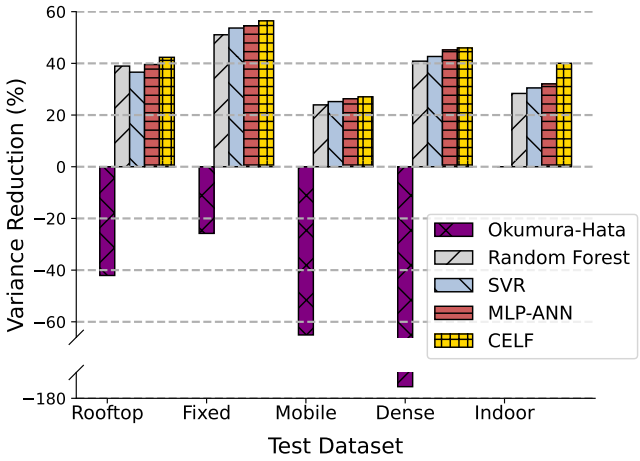


Fig. 6: Variance reductions on the outdoor and indoor test datasets via *Okumura-Hata*, three ML methods, and CELF.

datasets. Note that the *Okumura-Hata* model predicts path loss directly without first-order channel estimation and thus its error variance is computed as the *unbiased path loss variance*. It can be seen from Fig. 6 that all methods except the *Okumura-Hata model* can lower the fading loss variance to a certain degree. MLP-ANN gives the largest variance reduction among the three ML-based methods. However, CELF outperforms all the ML models across the test datasets. Take the *Rooftop* dataset for instance. CELF can achieve 42.3% variance reduction which is higher than MLP-ANN's 39.6%. To summarize, we are able to show that the CELF algorithm outperforms the three ML methods in terms of variance reduction.

### C. Efficiency analysis

We compare the training and testing efficiency of the methods via running time. Their results are shown in Table III. First, it can be observed that the *Okumura-Hata model* provides the fastest predictions due to its closed-form computation. Second, MLP-ANN, among the remaining methods, is the most efficient for shadowing loss prediction but the most computationally expensive for training. Third, the slowest model for testing is SVR except for the indoor dataset. Last, CELF is approximately 3 times faster than MLP-ANN for image learning. As a result, it can update the model with new measurements or learn the spatial loss of a new environment with much less computational cost. Comparing the prediction

| Receiver | Data Variance ($dB^2$) | | | Reduction |
|---|---|---|---|---|
| | Stationary | Radius$\leq 1\lambda_f$ | Sum | Percentage |
| Rooftop | 3.9 | 20.3 | 24.3 | 58.4% |
| Fixed | 2.9 | 11.0 | 13.9 | 76.9% |
| Dense | 2.6 | 8.2 | 10.8 | 58.8% |

TABLE IV: Data variance when the portable transmitter is stationary or rotating with a radius $\leq 1\lambda_f$.

time, we can see that CELF is slower than MLP-ANN across all the datasets. This is due to the time-expensive weight matrix computation for each data point. Optimization of the weight model is needed for prediction efficiency improvement and remains future work.

### D. Effect of hyperparameters

CELF's hyperparameters play a significant role in its performance. We here present variance reduction as a function of CELF's three major hyperparameters on the indoor dataset.

Fig. 7a shows that the variances for both training and test datasets mostly reduce less as the pixel width $\delta_p$ increases from 0.15m to 15m. Fluctuations occur at near 2.5 m, 3.5 m, 5 m, and 8 m. While the lower the pixel width, the higher the variance reduction, it comes with a training time sacrifice. Fig. 7b discusses the reduction variation vs. the space constant $\delta$. Reductions for testing and training decrease as $\delta$ increase from 0.5m to 15m. As $\delta$ approximates the obstruction size, unreasonable large space constants give lower variance reduction for training and testing. Fig. 7c presents the effect of the excess length $\lambda$ on variance reduction. It can be seen that too large of the excess length includes too many pixels for loss field estimation and thus leads to lower variance reduction.

### E. Lower variance bound approximation

We analyze a subset of the outdoor dataset which is collected when the FM transmitter is either stationary or rotating with a radius less than or equal to 1 wavelength ($\lambda_f$). The subset has 14,026 received power observations. Variation in stationary data approximates the measurement noise variance, and the data for link distances changing on the order of the signal wavelength can estimate the small-scale fading loss [20]. Hence the sum of the two gives a sense of the lower bound on the total fading loss variance $\sigma_{\boldsymbol{n}}^2$. Table IV illustrates the variance of the two measurement sets. Note that the *Mobile* dataset is not applicable as the receivers are constantly moving. We can learn that for the *Dense* dataset, the variance reduction

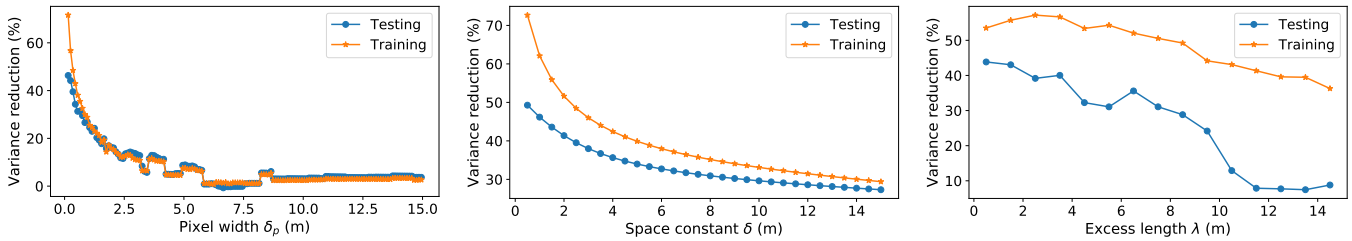


(a) The effect of the pixel width $\delta_p$. (b) The effect of the space constant $\delta$. (c) The effect of the excess length $\lambda$.

Fig. 7: Variance reduction vs. CELF's hyperparameters on the indoor dataset.

upper limit is 58.8% which, based on Fig. 6, is 12.9% higher than the result of CELF. By comparing Table IV and Fig. 6, we can conclude that there is still room to lower the shadowing loss variance, but the proposed method has shown results closer to the limits.

## VI. Conclusion

This paper proposes CELF, which learns a spatial loss field and uses it to predict shadowing loss on any new links in a deployment area. It formulates total fading loss via a discretized linear model and applies Bayesian linear regression and optimization for the loss image estimation.

The proposed method has been validated with two evaluation metrics, variance reduction, and running time for training and prediction. It is tested on one outdoor and one indoor real-world dataset. The *Okumura-Hata* model and three ML-based methods, SVR, random forest, and MLP-ANN, are used for performance comparison. Experimental results demonstrate that CELF presents larger variance reductions than all the other methods and can also estimate the loss image more efficiently than the most accurate MLP-ANN model.

## References


[1] W. S. H. M. W. Ahmad, N. A. M. Radzi, F. Samidi, A. Ismail, F. Abdullah, M. Z. Jamaludin, and M. Zakaria, "5G technology: Towards dynamic spectrum sharing using cognitive radio networks," *IEEE Access*, vol. 8, pp. 14 460–14 488, 2020.

[2] S. Bhattarai, J.-M. J. Park, B. Gao, K. Bian, and W. Lehr, "An overview of dynamic spectrum sharing: Ongoing initiatives, challenges, and a roadmap for future research," *IEEE Transactions on Cognitive Communications and Networking*, vol. 2, no. 2, pp. 110–128, 2016.

[3] M. M. Sohul, M. Yao, T. Yang, and J. H. Reed, "Spectrum access system for the citizen broadband radio service," *IEEE Communications Magazine*, vol. 53, no. 7, pp. 18–25, 2015.

[4] T. Kidd, "National radio quiet and dynamic zones," in *CHIPS: The Department of the Navy's Information Technology Magazine*, 2018. [Online]. Available: https://www.doncio.navy.mil/chips/ArticleDetails.aspx?ID=10299

[5] M. Zheleva, C. R. Anderson, M. Aksoy, J. T. Johnson, H. Affinnih, and C. G. DePree, "Radio dynamic zones: Motivations, challenges, and opportunities to catalyze spectrum coexistence," *IEEE Communications Magazine*, vol. 61, no. 6, pp. 156–162, 2023.

[6] D. Eppink and W. Kuebler, "TIREM/SEM handbook," *Defense Technical Information Center*, 1994.

[7] Z. Yun and M. F. Iskander, "Ray tracing for radio propagation modeling: Principles and applications," *IEEE Access*, vol. 3, pp. 1089–1100, 2015.

[8] M. Hata, "Empirical formula for propagation loss in land mobile radio services," *IEEE Transactions on Vehicular Technology*, vol. 29, no. 3, pp. 317–325, 1980.

[9] T. S. Rappaport, *Wireless communications: Principles and practice, 2/E*. Pearson, 2010.

[10] A. Clegg, "Google and CBRS," https://www.youtube.com/watch?v=2vxjFDieP1Q, Sept. 2019, Speech at NEDAS 2019 NYC Summit.

[11] A. Seretis and C. D. Sarris, "An overview of machine learning techniques for radiowave propagation modeling," *IEEE Transactions on Antennas and Propagation*, vol. 70, no. 6, pp. 3970–3985, 2021.

[12] R. Levie, Ç. Yapar, G. Kutyniok, and G. Caire, "RadioUNet: Fast radio map estimation with convolutional neural networks," *IEEE Transactions on Wireless Communications*, vol. 20, no. 6, pp. 4001–4015, 2021.

[13] J. Gerlings, A. Shollo, and I. Constantiou, "Reviewing the need for explainable artificial intelligence (xAI)," *Proceedings of the Hawaii Intl. Conf. System Sciences (HICSS) 54*, 2020, arXiv preprint arXiv:2012.01007.

[14] A. Holzinger, C. Biemann, C. S. Pattichis, and D. B. Kell, "What do we need to build explainable ai systems for the medical domain?" *arXiv preprint arXiv:1712.09923*, 2017.

[15] J. Wilson and N. Patwari, "Radio tomographic imaging with wireless networks," *IEEE Transactions on Mobile Computing*, vol. 9, no. 5, pp. 621–632, 2010.

[16] C. R. Karanam and Y. Mostofi, "3D through-wall imaging with unmanned aerial vehicles using WiFi," in *Proceedings of the 16th ACM/IEEE Intl. Conf. Information Processing in Sensor Networks*, 2017, pp. 131–142.

[17] J. Wang and N. Patwari, "Git repository of the proposed channel estimation via loss field (CELF) model," https://gitlab.flux.utah.edu/Jie_Wang/channel-estimation-via-loss-field, 2024.

[18] H. Hashemi, "The indoor radio propagation channel," *Proceedings of the IEEE*, vol. 81, no. 7, pp. 943–968, 1993.

[19] C. Phillips, D. Sicker, and D. Grunwald, "A survey of wireless path loss prediction and coverage mapping methods," *IEEE Communications Surveys & Tutorials*, vol. 15, no. 1, pp. 255–270, 2012.

[20] A. Goldsmith, *Wireless communications*. Cambridge Univ. Press, 2005.

[21] A. Hrovat, G. Kandus, and T. Javornik, "A survey of radio propagation modeling for tunnels," *IEEE Communications Surveys & Tutorials*, vol. 16, no. 2, pp. 658–669, 2013.

[22] J. S. Seybold, *Introduction to RF propagation*. John Wiley & Sons, 2005.

[23] G. A. Hufford, A. G. Longley, W. A. Kissick *et al.*, *A guide to the use of the ITS irregular terrain model in the area prediction mode*. US Department of Commerce, National Telecommunications and Information Administration, 1982.

[24] M. R. Souryal and T. T. Nguyen, "Effect of federal incumbent activity on CBRS commercial service," in *2019 IEEE Intl. Symposium on Dynamic Spectrum Access Networks (DySPAN)*, 2019, pp. 1–5.

[25] M. A. Varner, F. Mitchell, J. Wang, K. Webb, and G. D. Durgin, "Enhanced RF modeling accuracy using simple minimum mean-squared error correction factors," in *2022 IEEE 2nd Intl. Conf. Digital Twins and Parallel Intelligence (DTPI)*, 2022, pp. 1–5.

[26] P. Series, *Recommendation ITU-R P.1812-6: A path-specific propagation prediction method for point-to-area terrestrial services in the frequency range 30 MHz to 6000 MHz*. International Telecommunication Union, 2021.

[27] S. S. Szyszkowicz, H. Yanikomeroglu, and J. S. Thompson, "On the feasibility of wireless shadowing correlation models," *IEEE Transactions on Vehicular Technology*, vol. 59, no. 9, pp. 4222–4236, 2010.

[28] J. Lee and F. Baccelli, "On the effect of shadowing correlation on wireless network performance," in *IEEE INFOCOM*, 2018, pp. 1601–1609.

[29] N. Patwari and P. Agrawal, "Nesh: A joint shadowing model for links in a multi-hop network," in *2008 IEEE Intl. Conf. Acoustics, Speech and Signal Processing*, 2008, pp. 2873–2876.

[30] A. Abdi and M. Kaveh, "On the utility of gamma pdf in modeling shadow fading (slow fading)," in *1999 IEEE 49th Vehicular Technology Conference*, vol. 3, 1999, pp. 2308–2312.

[31] P. Ramírez-Espinosa and F. J. Lopez-Martinez, "Composite fading models based on inverse gamma shadowing: Theory and validation," *IEEE Transactions on Wireless Communications*, vol. 20, no. 8, pp. 5034–5045, 2021.

[32] H.-S. Jo, C. Park, E. Lee, H. K. Choi, and J. Park, "Path loss prediction based on machine learning techniques: Principal component analysis, artificial neural network, and Gaussian process," *Sensors*, vol. 20, no. 7, p. 1927, 2020.

[33] Y. Zhang, J. Wen, G. Yang, Z. He, and J. Wang, "Path loss prediction based on machine learning: Principle, method, and data expansion," *Applied Sciences*, vol. 9, no. 9, p. 1908, 2019.

[34] L. Wu, D. He, B. Ai, J. Wang, H. Qi, K. Guan, and Z. Zhong, "Artificial neural network based path loss prediction for wireless communication network," *IEEE Access*, vol. 8, pp. 199 523–199 538, 2020.

[35] E. Ostlin, H.-J. Zepernick, and H. Suzuki, "Macrocell path-loss prediction using artificial neural networks," *IEEE Transactions on Vehicular Technology*, vol. 59, no. 6, pp. 2735–2747, 2010.

[36] S. Ojo, A. Imoize, and D. Alienyi, "Radial basis function neural network path loss prediction model for LTE networks in multitransmitter signal propagation environments," *Intl. Journal of Communication Systems*, vol. 34, no. 3, p. e4680, 2021.

[37] J. Thrane, D. Zibar, and H. L. Christiansen, "Model-aided deep learning method for path loss prediction in mobile communication systems at 2.6 GHz," *IEEE Access*, vol. 8, pp. 7925–7936, 2020.

[38] C. Bettstetter and C. Hartmann, "Connectivity of wireless multihop networks in a shadow fading environment," in *Proc. 6th ACM Workshop on Modeling Analysis & Simulation of Wireless & Mobile Systems*, 2003, pp. 28–32.

[39] R. Hekmat and P. Van Mieghem, "Connectivity in wireless ad-hoc networks with a log-normal radio model," *Mobile Networks & Applications*, vol. 11, pp. 351–360, 2006.

[40] Y. Chen and A. Terzis, "On the implications of the log-normal path loss model: an efficient method to deploy and move sensor motes," in *ACM SenSys*, 2011, pp. 26–39.

[41] M. Gudmundson, "Correlation model for shadow fading in mobile radio systems," *Electronics letters*, vol. 23, no. 27, pp. 2145–2146, 1991.

[42] P. Agrawal and N. Patwari, "Correlated link shadow fading in multi-hop wireless networks," *IEEE Transactions on Wireless Communications*, vol. 8, no. 8, pp. 4024–4036, 2009.

[43] N. Patwari and P. Agrawal, "Effects of correlated shadowing: Connectivity, localization, and RF tomography," in *2008 Intl. Conf. Information Processing in Sensor Networks (IPSN 2008)*, 2008, pp. 82–93.

[44] G. D. Durgin, T. S. Rappaport, and D. A. de Wolf, "New analytical models and probability density functions for fading in wireless communications," *IEEE Trans. Communications*, vol. 50, no. 6, pp. 1005–1015, June 2002.

[45] G. H. Golub and C. F. Van Loan, *Matrix computations*. JHU Press, 2013.

[46] R. Garnett, *Bayesian optimization*. Cambridge Univ. Press, 2023.

[47] F. Mitchell, "The FRS/GMRS outdoor received power dataset," https://zenodo.org/record/7259895\#.ZDbPiezML0p, 2022.

[48] J. Breen, A. Buffmire, J. Duerig, K. Dutt, E. Eide, M. Hibler, D. Johnson, S. K. Kasera, E. Lewis, D. Maas, A. Orange, N. Patwari, D. Reading, R. Ricci, D. Schurig, L. B. Stoller, J. Van der Merwe, K. Webb, and G. Wong, "POWDER: Platform for open wireless data-driven experimental research," in *Proc. 14th Intl. Workshop on Wireless Network Testbeds, Experimental Evaluation and Characterization (WiNTECH)*, Sep. 2020.

[49] N. Patwari, "Indoor channel impulse response dataset," https://crawdad.org/utah/CIR/20070910/matlab/, 2022.

[50] N. Patwari, A. O. Hero, M. Perkins, N. S. Correal, and R. J. O'dea, "Relative location estimation in wireless sensor networks," *IEEE Transactions on Signal Processing*, vol. 51, no. 8, pp. 2137–2148, 2003.

[51] A. Marey, M. Bal, H. F. Ates, and B. K. Gunturk, "PL-GAN: Path loss prediction using generative adversarial networks," *IEEE Access*, vol. 10, pp. 90 474–90 480, 2022.

[52] J. Wen, Y. Zhang, G. Yang, Z. He, and W. Zhang, "Path loss prediction based on machine learning methods for aircraft cabin environments," *IEEE Access*, vol. 7, pp. 159 251–159 261, 2019.

[53] E. F. Drocella, J. Richards, R. Sole, F. Najmy, A. Lundy, and P. McKenna, "3.5 GHz exclusion zone analyses and methodology," National Telecommunications and Information, Tech. Rep., 2016.

[54] C. A. Oroza, Z. Zhang, T. Watteyne, and S. D. Glaser, "A machine-learning-based connectivity model for complex terrain large-scale low-power wireless deployments," *IEEE Transactions on Cognitive Communications and Networking*, vol. 3, no. 4, pp. 576–584, 2017.

[55] N. Moraitis, L. Tsipi, and D. Vouyioukas, "Machine learning-based methods for path loss prediction in urban environment for LTE networks," in *2020 16th Intl. Conf. Wireless and Mobile Computing, Networking and Communications (WiMob)*, 2020, pp. 1–6.

[56] G. D. Durgin, M. A. Varner, N. Patwari, S. K. Kasera, and J. Van der Merwe, "Digital spectrum twinning for next-generation spectrum management and metering," in *2022 IEEE 2nd Intl. Conf. Digital Twins and Parallel Intelligence (DTPI)*, 2022, pp. 1–6.